Available online at www.sciencedirect.com
SCIENCE DIRECT®
Journal of Computational Physics 205 (2005) 269–291
JOURNAL OF COMPUTATIONAL PHYSICS
www.elsevier.com/locate/jcp

Modelling thermal convection with large viscosity gradients in one block of the 'cubed sphere'

Gaël Choblet *

Laboratoire de planétologie et géodynamique, UMR-CNRS 6112, Université de Nantes, Faculté des sciences et des techniques, 2, rue de la Houssiniere, BP 92208, 44322 Nantes Cedex 3, France

Received 29 July 2004; received in revised form 3 November 2004; accepted 8 November 2004
Available online 10 December 2004

Abstract

A numerical method solving thermal convection problems with variable viscosity in a spherical shell is presented. Several features of earlier programs solving the same problem in Cartesian geometry are adopted because of their efficiency and robustness: finite volume formulation, multigrid flow solver, parallel implementation. A recent composite mesh gridding technique for a spherical surface, termed the 'cubed sphere', has proven to be successful in solving other partial differential equations in geophysical problems. It is used here because of its various advantages: absence of geometrical singularities, same metric on each block, simple coupling of adjacent blocks. In addition, it is a good tool to implement grid-based methods proven efficient in the Cartesian context since it provides a mesh reasonably close to uniform. Although as in the Cartesian case, convergence rates decrease with increasing viscosity gradients, global contrasts up to 10^6 are obtained at a reasonable cost.

Keywords: Spherical geometry; Multigrid methods; Thermal convection; Variable viscosity

1. Introduction

Describing the thermal history and internal dynamics of terrestrial planets involves the understanding of heat transfer through thermal convection associated to solid creep on geological time scales (e.g. [22]). The effective viscosity controlling diffusion of momentum in silicate mantles or icy layers within satellites of giant planets is large enough compared to the diffusion of heat to neglect inertial terms in the Navier–Stokes equations. However, viscosity of planetary materials is also very sensitive to thermodynamical parameters

* Tel.: +33 2 5112 5480; fax: +33 2 5112 52.
E-mail address: choblet@chimie.univ-nantes.fr.

0021-9991/$ - see front matter © 2004 Elsevier Inc. All rights reserved.
doi:10.1016/j.jcp.2004.11.005

such as temperature, and to a lesser extent, pressure. Variations of several orders of magnitude are predicted for both ice and silicates. Strongly temperature-dependent viscosity tends to build up a cold conductive lid on top of the convective layer, a regime that is now well understood (e.g. [19]). In order to mimic the plate behavior, more complex rheologies have been proposed (see for examples the articles of Tackley [24,25]; and see Bercovici [5] for a synthesis). These new models also require flow solvers handling large viscosity gradients that tend to complicate the numerical resolution. Recent progress in the treatment of 3D numerical models of convection designed for planetary interiors have thus focused on fast methods that can handle large viscosity gradients (e.g. [1,10,23]). Multigrid methods with a finite-volume (-difference) formulation have been proved to provide the most efficient (fast and robust) methods to solve thermal convection problems with large viscosity gradients in a 3D Cartesian box (e.g. [1]).

Several of today's questions in the study of planetary interiors now also imply the use of models adapted to a spherical geometry whether this is implicitly required by the internal dynamics or due to a better comparison of these with geophysical data often expressed as a decomposition into spherical harmonics (e.g. in the case of data from space exploration). The use of a spherical harmonics decomposition was indeed the first solution proposed for solving the thermal convection problems with spectral methods [6]. However, lateral variations of viscosity forbid the use of the simple, potential-derived, formulation proposed by Chandrasekhar [9] so that the Legendre transform turns out to be rather expensive when compared to finite volume methods... In addition, a comparison with finite volume methods indicates that spectral methods lead to inaccurate results when dealing with large viscosity gradients [1]. A first attempt to solve variable viscosity convection in a spherical geometry with a grid-based method is proposed by Hsui et al. [13] after a finite element discretization developed in the isoviscous case (program Terra) by Baumgardner [4]. Finite volume methods were also proposed for a mesh corresponding to classical spherical coordinates [17]: moderate viscosity contrasts of several tens were reached. Another finite-element program termed CITCOMs presented in Zhong et al. [30] is to the author's knowledge the most efficient model for thermal convection with variable viscosity. It uses a multigrid algorithm for the flow solver. The spherical shell is divided into 12 blocks of approximately equal size, thus allowing an efficient parallel implementation. Global viscosity contrasts up to 10^4 were treated.

Recently, a new gridding technique termed the 'cubed sphere' method is developed by Ronchi et al. [18] based on the projection of a cube on the circumscribed sphere, leading to a decomposition into six identical regions. Due to coordinate singularities, composite mesh methods are needed when dealing with a spherical geometry. A classical drawback of this approach however, is the interpolation procedure in the coupling of the different meshes, sometimes representing a significant part of the global computation time. Ronchi et al. [18] show that the six meshes constituting the cubed sphere are 'stably and accurately coupled performing interpolations only in one dimension and using a minimum amount of overlap'. In addition to be free of singularities, this grid is reasonably close to a uniform mesh and defines a single metric for the six regions. Thus, this gridding technique allows the use of standard grid-based algorithms developed for regular meshes. It has been implemented in the field of solid Earth physics to describe wave propagation in a heterogeneous Earth [8,15]. A first successful application to isoviscous thermal convection at an infinite Prandtl number is proposed by Hernlund and Tackley [12].

Here, I develop a solution for 3D convection in the case of a spherical shell using the cubed sphere method and implementing the techniques proved to be most efficient in the Cartesian case. I derive the equations in the cubed sphere, curvilinear coordinate system, and propose a discretization technique with an implementation using a multigrid algorithm suitable for computation on parallel architecture. As a first step, the program is designed to solve the problem in only one sixth of the spherical shell (corresponding to the radial extension of one single block of the cubed sphere): many of the convection problems requiring the spherical geometry can indeed be solved in a domain with a finite angular extent. For example, the strong influence of curvature on the stability of the hot boundary layer can be assessed more easily since a smaller domain allows more systematic calculations. Such a curved region could also be treated easily by more simple orthogonal coordinate systems and the main interest of the cubed sphere mesh is certainly that it provides

a simple and efficient treatment of the whole sphere: this is the ultimate goal of the present program. The extension of the present version to the whole shell is mainly a problem of computation size for grid meshes adapted to the convective regimes of planetary interiors. Since all six regions are similar, the developments proposed in the present article are directly suitable to the treatment of the whole sphere in a future version of the program. The present article mainly focuses on the flow solver: a specific study benchmarking advection schemes for the equation describing the conservation of energy will be the object of a subsequent article.

2. Governing equations

2.1. Thermal convection with variable viscosity

The problem solved by this program is the natural thermal convection of a viscous incompressible fluid with a strongly temperature-dependent viscosity for an infinite Prandtl number in the Boussinesq approximation (except for the variable viscosity) so that the set of conservation equations (mass, Eq. (1); momentum, Eq. (2); energy, Eq. (3)) describing the flow is the following in its dimensionless form:

$$\overline{\nabla}\cdot\bar{V}=0, \tag{1}$$

$$\bar{0}=-\overline{\nabla}p+\overline{\nabla}\cdot\left[\mu\left(\overline{\nabla}\bar{V}+\left(\overline{\nabla}\bar{V}\right)^{\mathrm{T}}\right)\right]+Ra\theta\bar{\gamma}_r, \tag{2}$$

$$\frac{\mathrm{D}\theta}{\mathrm{D}t}=\nabla^2\theta+\tilde{H} \tag{3}$$

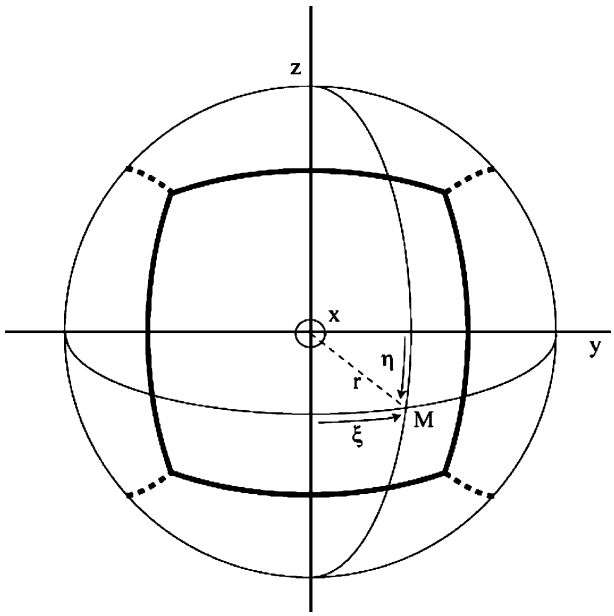

Fig. 1. The 'cubed sphere' coordinate system (r,ξ,η). Point M located on a sphere of radius r is referenced by angular coordinates ξ and η associated to two great circles corresponding to a vertical line (ξ) and a horizontal line (η) on the surface. The region we study with these coordinates (delimited by bold lines; other blocks' limits are indicated by bold dashed lines) intersects the sphere through a sixth of the surface defined by the following range for both ξ and η: $[-\pi/4,\pi/4]$. The Cartesian coordinates system (x,y,z) is also displayed as a reference (with the x-direction orthogonal to the figure's plane).

with $\bar{V}$ the velocity vector; p the pressure; μ the dynamic viscosity; θ the temperature; $\bar{\gamma}_r$ a vertical unit vector; $\tilde{H}$ the dimensionless volumetric heating rate. Viscous heating is neglected in the energetic budget. The characteristic scales are the following: time $[t] = d^2/\kappa$, diffusive time scale with κ, thermal diffusivity; viscosity $[\mu] = \mu_0$, viscosity value for the surface temperature T_0; length $[L] = d = R_t - R_b = R_t(1-\rho)$, thickness of the fluid shell (with R_t radius of the outer sphere, R_b radius of the inner sphere, and $\rho = R_b/R_t$).

Two alternative scales are proposed for temperature, depending on the bottom boundary condition. If a heat flux f_b is prescribed, the characteristic temperature difference is $\Delta T_f = (f_b + Hd)d/k$ with H volumetric heating rate and k thermal conductivity. If a temperature T_b is prescribed, I use $\Delta T_T = T_b - T_0$ (temperature is prescribed at the surface in all models). The dimensionless temperature field θ associated to ΔT_f is noted θ_f, the one associated to ΔT_T is θ_T. The two Rayleigh numbers are Ra_f and Ra_T:

$$Ra_f = \frac{\alpha\rho_0 g(f_b + Hd)d^4}{k\kappa\mu_0}, \tag{4a}$$

$$Ra_T = \frac{\alpha\rho_0 g\Delta T_T d^3}{\kappa\mu_0} \tag{4b}$$

with α the thermal expansion; ρ_0 the reference density; g the acceleration due to gravity. Since there is no unique way to define the Rayleigh number for a non-uniform viscosity field, I propose the use of the constant viscosity value μ_0 (thus, the Rayleigh number value is not fully characteristic of the convective flow in the cell's interior).

For simplicity, the temperature-dependence of viscosity is chosen to be exponential so that dimensionless viscosity is

$$\tilde{\mu} = \exp(-a_{\text{vis}}\theta). \tag{5}$$

This choice is commonly used to describe viscosity of silicate rocks (Frank–Kamenetskii approximation) [20].

2.2. The '*cubed sphere*' coordinates system

The 'cubed sphere' method proposed by Ronchi et al. [18] is first designed to avoid coordinate singularities at the poles. Other interesting aspects of the method are: (i) the fact that the physical grid defined on the spherical surface is reasonably close to a uniform grid; (ii) the decomposition of the spherical shell into six identical regions, with the same metric; (iii) an efficient parallel implementation.

The mapping of the spherical surface is obtained by the projection of the sides of a circumscribed cube onto this surface. Fig. 1 illustrates this technique and introduces the 'cubed sphere' coordinate system (r,ξ,η). Note that it is not an orthogonal system since the vertical great circles intersect orthogonally only with the equator (and the η = constant great circles with the $\xi = 0$ meridian). In addition it appears that angular coordinates ξ and η are such that a symmetry between them is expected in all the following calculations. Tensor algebra is proposed in order to explicitly write the equations in this coordinate system, thus avoiding the computation of the metric tensor elements during the numerical computation. As proposed by Ronchi et al. [18], the following auxiliary variables will be introduced in order to simplify the expressions of differential operators:

$$\begin{aligned}
X &\equiv \tan\xi = \frac{y}{x},\\
Y &\equiv \tan\eta = \frac{z}{x},\\
\delta &\equiv 1 + X^2 + Y^2 = 1 + \left(\frac{y}{x}\right)^2 + \left(\frac{z}{x}\right)^2,\\
C &\equiv \sqrt{1+X^2} = \sqrt{1 + \left(\frac{y}{x}\right)^2},\\
D &\equiv \sqrt{1+Y^2} = \sqrt{1 + \left(\frac{z}{x}\right)^2}
\end{aligned} \tag{6}$$

(The relationships with Cartesian coordinates (x,y,z) for one of the equatorial blocks are provided as an indication.) In Appendix A, I develop analytical calculations of the coordinate system for one sixth of the spherical shell and the detailed derivations of Eqs. (1)–(3). The conservation of mass is

$$\frac{1}{r^2}\left(r^2\tilde{V}^r\right)_{,r}+\frac{\delta^{3/2}}{rDC^2}\left(\frac{\tilde{V}^\xi}{\delta^{1/2}}\right)_{,\xi}+\frac{\delta^{3/2}}{rCD^2}\left(\frac{\tilde{V}^\eta}{\delta^{1/2}}\right)_{,\eta}=0 \tag{7}$$

where $(\tilde{V}^r,\tilde{V}^\xi,\tilde{V}^\eta)$ are the contravariant components of the velocity vector in the physical basis associated to (r,ξ,η). One important step toward the Stokes equations is the expression of the stress tensor; the contravariant components in the physical basis are the following:

$$\begin{aligned}
\tilde{\tau}^{rr}&=2\mu\tilde{V}^r_{,r},\\
\tilde{\tau}^{r\xi}&=\mu\left(r\left(\frac{\tilde{V}^\xi}{r}\right)_{,r}+\frac{D}{r}\tilde{V}^r_{,\xi}+\frac{XY}{rD}\tilde{V}^r_{,\eta}\right),\\
\tilde{\tau}^{r\eta}&=\mu\left(r\left(\frac{\tilde{V}^\eta}{r}\right)_{,r}+\frac{C}{r}\tilde{V}^r_{,\eta}+\frac{XY}{rC}\tilde{V}^r_{,\xi}\right),\\
\tilde{\tau}^{\xi\xi}&=2\mu\left(\frac{XY}{r\delta^{1/2}}\left(\frac{\sqrt{\delta}\tilde{V}^\xi}{D}\right)_{,\eta}+\frac{D}{r}\tilde{V}^\xi_{,\xi}+\frac{C^2D^2}{r\delta}\tilde{V}^r+\frac{-CYD^2}{r\delta}\tilde{V}^\eta\right),\\
\tilde{\tau}^{\xi\eta}&=\mu\left(\frac{CD}{r\delta^{1/2}}\left(\frac{\sqrt{\delta}\tilde{V}^\eta}{C}\right)_{,\xi}+\frac{-XYCD}{\delta}\tilde{V}^r_{,r}+\frac{CD}{r\delta^{1/2}}\left(\frac{\sqrt{\delta}\tilde{V}^\xi}{D}\right)_{,\eta}\right),\\
\tilde{\tau}^{\eta\eta}&=2\mu\left(\frac{XY}{r\delta^{1/2}}\left(\frac{\sqrt{\delta}\tilde{V}^\eta}{C}\right)_{,\xi}+\frac{C}{r}\tilde{V}^\eta_{,\eta}+\frac{C^2D^2}{r\delta}\tilde{V}^r-\frac{DXC^2}{r\delta}\tilde{V}^\xi\right).
\end{aligned} \tag{8}$$

The three projections of the conservation of momentum are

$$-p_{,r}+\frac{1}{r^3}\left(r^3\tilde{\tau}^{rr}\right)_{,r}+\frac{\delta^{3/2}}{rCD^2}\left(\frac{\tilde{\tau}^{r\eta}}{\delta^{1/2}}\right)_{,\eta}+\frac{\delta^{3/2}}{rC^2D}\left(\frac{\tilde{\tau}^{r\xi}}{\delta^{1/2}}\right)_{,\xi}+f_r=0, \tag{9a}$$

$$\frac{-1}{r}\left(\frac{XY}{D}p_{,\eta}+Dp_{,\xi}\right)+\frac{1}{r^3}\left(r^3\tilde{\tau}^{\xi r}\right)_{,r}+\frac{\delta^{3/2}}{rC^2D}\left(\frac{\tilde{\tau}^{\xi\xi}}{\delta^{1/2}}\right)_{,\xi}+\frac{\delta^{3/2}}{rCD}\left(\frac{\tilde{\tau}^{\xi\eta}}{D\delta^{1/2}}\right)_{,\eta}=0, \tag{9b}$$

$$\frac{-1}{r}\left(\frac{XY}{C}p_{,\xi}+Cp_{,\eta}\right)+\frac{1}{r^3}\left(r^3\tilde{\tau}^{\eta r}\right)_{,r}+\frac{\delta^{3/2}}{rCD^2}\left(\frac{\tilde{\tau}^{\eta\eta}}{\delta^{1/2}}\right)_{,\eta}+\frac{\delta^{3/2}}{rCD}\left(\frac{\tilde{\tau}^{\eta\xi}}{C\delta^{1/2}}\right)_{,\xi}=0. \tag{9c}$$

Finally, the conservation of energy is

$$\theta_{,t}+\theta_{,r}\tilde{V}^r+\frac{\delta}{rC^2D}\theta_{,\xi}\tilde{V}^\xi+\frac{\delta}{rCD^2}\theta_{,\eta}\tilde{V}^\eta=\frac{1}{r^2}\left(r^2\theta_{,r}\right)_{,r}+\frac{\delta}{r^2}\left[\frac{\theta_{,\xi\xi}}{C^2}+\frac{\theta_{,\eta\eta}}{D^2}+\frac{2XY}{C^2D^2}\theta_{,\xi\eta}\right]+\tilde{H}. \tag{10}$$

3. Numerical method

3.1. Finite volume discretization

The surface defined above (Fig. 1) is then mapped onto a 'rectangular' grid, where the equations are solved using a standard finite volumes technique designed for regular meshes. The gridding technique can be illustrated by two sets of great circles spaced with a uniform angular increment ($\Delta\xi$ and $\Delta\eta$) for ξ and η varying between $-\pi/4$ and $\pi/4$. The mesh is then extended radially between the two spherical surfaces bounding the shell ($r = \rho$) and ($r = 1$), by concentric spheres with identical angular discretization, spaced by a radius increment Δr. The curved numerical domain is thus divided into non-uniform cells C_{ijk} (i, j and k, corresponding to the indixes in the r-, ξ- and η-directions, respectively, see Fig. 2). The staggered grid mesh approach is adopted as commonly used in computations using primitive variables: pressure and temperature discrete values are positioned at volume cell centers and the three velocity components at the center of cell walls perpendicular to their direction (see the classical description by Harlow and Welch [11] for a Cartesian grid and by Wesseling [29] for an arbitrary grid). This prevents from artificial pressure oscillations and provides a good accuracy for the discrete scheme. In 3D Cartesian models, the staggered grid mesh formulation provides a relatively simple discretization of variable viscosity elliptic PDEs (1–3) (e.g. [23,10]). The discrete scheme is more complex for the curved layer due to the non-orthogonal coordinate system (r,η,ξ). Finally, the choice is made to use contravariant coordinates providing a better evaluation of fluxes in the case of a staggered grid.

3.1.1. Mass conservation

In the following, discrete values for pressure, temperature, viscosity and velocity variables always refer to dimensionless values and contravariant coordinates in the normed physical basis. See Appendix B for fur-

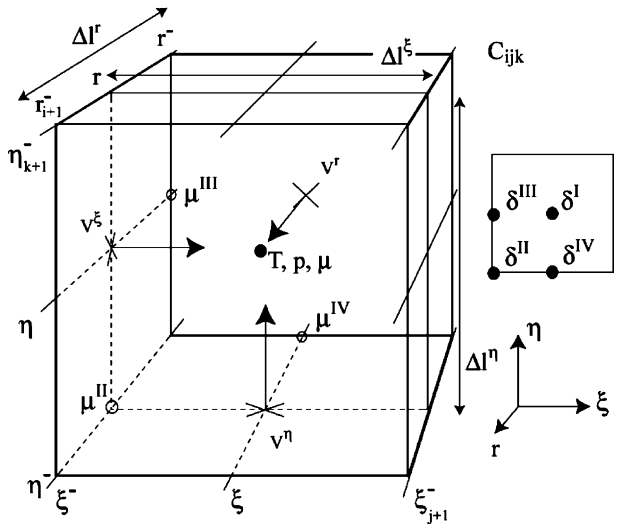

Fig. 2. Locations and notations for the discrete values in the staggered grid mesh approach for cell C_{ijk}. The black dot in the center of the cell (coordinates: r,ξ,η) refer to the location of temperature, pressure and viscosity. X symbols on the center of cell walls indicate the locations of velocity components. The coordinates of cell walls are r^-, ξ^-, η^-. Notations used in the discretization are also presented concerning angular variable $\delta = 1 + \tan^2\xi + \tan^2\eta$ (δ^{I}, δ^{II}, δ^{III}, δ^{IV}) and viscosity (μ^{II}, μ^{III}, μ^{IV}). See text in Appendix B for further details on these notations. The dimensions of the cell are Δl^r, Δl^ξ, Δl^η.

ther details on the discrete scheme's notations. Mass conservation equation (Eq. (8)) is written on a control volume matching the grid cell,

$$\frac{1}{r^2\Delta r}\left(r_{i+1}^{-2}V_{i+1}^{r}-r^{-2}V^{r}\right)+\frac{\delta^{I^{3/2}}}{rDC^2\Delta\xi}\left(\frac{V_{j+1}^{\xi}}{\sqrt{\delta_{j+1}^{\mathrm{III}}}}-\frac{V^{\xi}}{\sqrt{\delta^{\mathrm{III}}}}\right)+\frac{\delta^{I^{3/2}}}{rCD^2\Delta\eta}\left(\frac{V_{k+1}^{\eta}}{\sqrt{\delta_{k+1}^{\mathrm{IV}}}}-\frac{V^{\eta}}{\sqrt{\delta^{\mathrm{IV}}}}\right)=0 \tag{11}$$

where, unless expressly indicated, indexes values for the variables that vary in space are i, j, k (e.g. $V_{j+1}^{\xi}=V_{i,j+1,k}^{\xi}$, $\delta^{\mathrm{III}}=\delta_{j,k}^{\mathrm{III}}$).

3.1.2. Momentum conservation

For the conservation of momentum (Eqs. (9)), the control volumes are shifted, reflecting the location of velocity in the staggered grid mesh approach. In the r-direction (Eq. (9a)),

$$\begin{aligned}0=&\frac{-p+p_{i-1}}{\Delta r}+\frac{1}{r^{-3}\Delta r}\left(r^3\tau^{rr}-r_{i-1}^3\tau_{i-1}^{rr}\right)+\frac{\delta^{I^{3/2}}}{r^{-}CD^2\Delta\eta}\left(\frac{\tau_{k+1}^{r\eta}}{\sqrt{\delta_{k+1}^{\mathrm{IV}}}}-\frac{\tau^{r\eta}}{\sqrt{\delta^{\mathrm{IV}}}}\right)\\&+\frac{\delta^{I^{3/2}}}{r^{-}C^2D\Delta\xi}\left(\frac{\tau_{j+1}^{r\xi}}{\sqrt{\delta_{j+1}^{\mathrm{III}}}}-\frac{\tau^{r\xi}}{\sqrt{\delta^{\mathrm{III}}}}\right)+f_r\end{aligned} \tag{12}$$

with

$$\tau^{rr}=2\mu\frac{V_{i+1}^{r}-V^{r}}{\Delta r}, \tag{13}$$

$$\tau^{r\eta}=\mu^{\mathrm{IV}}\left(\frac{r^{-}}{\Delta r}\left(\frac{V^{\eta}}{r}-\frac{V_{i-1}^{\eta}}{r_{i-1}}\right)+\frac{C}{r^{-}\Delta\eta}\left(V^{r}-V_{k-1}^{r}\right)+\frac{XY^{-}}{r^{-}C\Delta\xi}\left(V_{j+1}^{r\mathrm{II}}-V^{r\mathrm{II}}\right)\right), \tag{14}$$

where $V^{r\mathrm{II}}=\frac{1}{4}(V^{r}+V_{j-1}^{r}+V_{k-1}^{r}+V_{j-1,k-1}^{r})$.

Similarly,

$$\tau^{r\xi}=\mu^{\mathrm{III}}\left(\frac{r^{-}}{\Delta r}\left(\frac{V^{\xi}}{r}-\frac{V_{i-1}^{\xi}}{r_{i-1}}\right)+\frac{D}{r^{-}\Delta\xi}\left(V^{r}-V_{j-1}^{r}\right)+\frac{X^{-}Y}{r^{-}D\Delta\eta}\left(V_{k+1}^{r\mathrm{II}}-V^{r\mathrm{II}}\right)\right). \tag{15}$$

Note that additional viscosity values μ^{III} and μ^{IV} interpolated from viscosities at cell centers are introduced (cf. Appendix B). This ensures the continuity of stress between adjacent cells, an important aspect when dealing with strongly variable coefficients [27].

Momentum conservation in the ξ-direction (Eq. (9b)),

$$\begin{aligned}0=&\frac{-1}{r}\left(\frac{X^{-}Y}{D\Delta\eta}\left(p_{k+1}^{\mathrm{II}}-p^{\mathrm{II}}\right)+\frac{D}{\Delta\xi}\left(p-p_{j-1}\right)\right)+\frac{1}{r^3\Delta r}\left(r_{i+1}^{-3}\tau_{i+1}^{\xi r}-r^{-3}\tau^{\xi r}\right)\\&+\frac{\delta^{\mathrm{III}^{3/2}}}{rC^{-2}D\Delta\xi}\left(\frac{\tau^{\xi\xi}}{\sqrt{\delta^{\mathrm{I}}}}-\frac{\tau_{j-1}^{\xi\xi}}{\sqrt{\delta_{j-1}^{\mathrm{I}}}}\right)+\frac{\delta^{\mathrm{III}^{3/2}}}{rC^{-}D\Delta\eta}\left(\frac{\tau_{k+1}^{\xi\eta}}{D_{k+1}^{-}\sqrt{\delta_{k+1}^{\mathrm{II}}}}-\frac{\tau^{\xi\eta}}{D^{-}\sqrt{\delta^{\mathrm{II}}}}\right)\end{aligned} \tag{16}$$

with $\tau^{\xi r}$ calculated with Eq. (15), and

$$\tau^{\xi\xi}=\frac{2\mu D^2}{r\delta^{\mathrm{I}}}\left(\frac{\sqrt{\delta^{\mathrm{I}}}XY}{D^2\Delta\eta}\left(\frac{\sqrt{\delta^{\mathrm{IV}}_{k+1}}V^{\xi\mathrm{IV}}_{k+1}}{D^-_{k+1}}-\frac{\sqrt{\delta^{\mathrm{IV}}}V^{\xi\mathrm{IV}}}{D^-}\right)+\frac{\delta^{\mathrm{I}}}{D\Delta\xi}\left(V^{\xi}_{j+1}-V^{\xi}\right)+C^2V^{r\mathrm{I}}-YCV^{\eta\mathrm{I}}\right) \tag{17}$$

where $V^{\xi\mathrm{IV}}=\frac{1}{4}(V^{\xi}+V^{\xi}_{j+1}+V^{\xi}_{k-1}+V^{\xi}_{j+1,k-1})$, $V^{r\mathrm{I}}=\frac{1}{2}(V^{r}+V^{r}_{i+1})$, $V^{\eta\mathrm{I}}=\frac{1}{2}(V^{\eta}+V^{\eta}_{k+1})$,

$$\tau^{\xi\eta}=\frac{\mu^{\mathrm{II}}C^-D^-}{r\sqrt{\delta^{\mathrm{II}}}}\left(\frac{1}{\Delta\xi}\left(\frac{\sqrt{\delta^{\mathrm{IV}}}V^{\eta}}{C}-\frac{\sqrt{\delta^{\mathrm{IV}}_{j-1}}V^{\eta}_{j-1}}{C_{j-1}}\right)+\frac{-rX^-Y^-}{\sqrt{\delta^{\mathrm{II}}}\Delta r}\left(V^{r-}_{i+1}-V^{r-}\right)+\frac{1}{\Delta\eta}\left(\frac{\sqrt{\delta^{\mathrm{III}}}V^{\xi}}{D}-\frac{\sqrt{\delta^{\mathrm{III}}_{k-1}}V^{\xi}_{k-1}}{D_{k-1}}\right)\right) \tag{18}$$

where $V^{r-}=\frac{1}{4}(V^{r}+V^{r}_{j-1}+V^{r}_{j-1,k-1}+V^{r}_{k-1})$.

Similarly, the momentum conservation in the η-direction (Eq. (9c)) is

$$\begin{aligned}0=&\frac{-1}{r}\left(\frac{XY^-}{C\Delta\xi}\left(p^{\mathrm{II}}_{j+1}-p^{\mathrm{II}}\right)+\frac{C}{\Delta\eta}\left(p-p_{k-1}\right)\right)+\frac{1}{r^3\Delta r}\left(r^{-3}_{i+1}\tau^{\eta r}_{i+1}-r^{-3}\tau^{\eta r}\right)\\&+\frac{\delta^{\mathrm{IV}^{3/2}}}{rCD^{-2}\Delta\eta}\left(\frac{\tau^{\eta\eta}}{\sqrt{\delta^{\mathrm{I}}}}-\frac{\tau^{\eta\eta}_{k-1}}{\sqrt{\delta^{\mathrm{I}}_{k-1}}}\right)+\frac{\delta^{\mathrm{IV}^{3/2}}}{rCD^-\Delta\xi}\left(\frac{\tau^{\xi\eta}_{j+1}}{C^-_{j+1}\sqrt{\delta^{\mathrm{II}}_{j+1}}}-\frac{\tau^{\xi\eta}}{C^-\sqrt{\delta^{\mathrm{II}}}}\right)\end{aligned} \tag{19}$$

with $\tau^{\eta r}$ and $\tau^{\xi\eta}$ calculated with Eqs. (14) and (18), respectively,

$$\tau^{\eta\eta}=\frac{2\mu C^2}{r\delta^{\mathrm{I}}}\left(\frac{\sqrt{\delta^{\mathrm{I}}}XY}{C^2\Delta\xi}\left(\frac{\sqrt{\delta^{\mathrm{III}}_{j+1}}V^{\eta\mathrm{III}}_{j+1}}{C^-_{j+1}}-\frac{\sqrt{\delta^{\mathrm{III}}}V^{\eta\mathrm{III}}}{C^-}\right)+\frac{\delta^{\mathrm{I}}}{C\Delta\eta}\left(V^{\eta}_{k+1}-V^{\eta}\right)+D^2V^{r\mathrm{I}}-DXV^{\xi\mathrm{I}}\right) \tag{20}$$

where $V^{\xi\mathrm{I}}=\frac{1}{2}(V^{\xi}+V^{\xi}_{j+1})$.

3.1.3. Energy conservation

Finally, the discrete form of the conservation of energy is

$$\begin{aligned}\frac{\theta^{n+1}-\theta^n}{\Delta t}+F^r+F^{\xi}+F^{\eta}=&\frac{1}{r^2\Delta r^2}\left[r_-^{j+1^2}(\theta_{i+1}-\theta)-r_-^2(\theta-\theta_{i-1})\right]\\&+\frac{\delta^{\mathrm{I}}}{r^2}\left[\frac{\theta_{j+1}-2\theta+\theta_{j-1}}{C^2\Delta\xi^2}+\frac{\theta_{k+1}-2\theta+\theta_{k-1}}{D^2\Delta\eta^2}+\frac{2XY\left(\theta_{j+1,k+1}-\theta_{j-1,k+1}-\theta_{j+1,k-1}+\theta_{j-1,k-1}\right)}{C^2D^2\Delta\xi\Delta\eta}\right]+\tilde{H}\end{aligned} \tag{21}$$

where all variables other than temperature are considered at time (n); advective fluxes F^r, F^{ξ}, F^{η} are computed using an improved upwind scheme [21]:

$$\begin{aligned}F^r&=\frac{1}{\Delta r}\left[\alpha^rV^r_{i+1}(\theta_{i+1}-\theta)+(1-\alpha^r)V^r(\theta-\theta_{i-1})\right],\\F^{\xi}&=\frac{\delta}{rC^2D\Delta\xi}\left[\alpha^{\xi}V^{\xi}_{j+1}\left(\theta_{j+1}-\theta\right)+\left(1-\alpha^{\xi}\right)V^{\xi}\left(\theta-\theta_{j-1}\right)\right],\\F^{\eta}&=\frac{\delta}{rCD^2\Delta\eta}\left[\alpha^{\eta}V^{\eta}_{k+1}(\theta_{k+1}-\theta)+(1-\alpha^{\eta})V^{\eta}(\theta-\theta_{k-1})\right],\end{aligned} \tag{22}$$

with coefficients $\alpha^{\bullet} = \frac{1}{1+e^{r^{\bullet}/2\Delta l^{\bullet}}}$; $\Delta l^{\bullet}$ is an infinitesimal displacement in the $\bullet$ direction (see Appendix B, Eq. (B.3)). Note that this simple explicit scheme is only first order in time. In addition, Hernlund and Tackley [12] mention the distortion of the temperature field associated to an anisotropic numerical dissipation associated to the context of non-orthogonal curvilinear coordinate systems. Thus, additional tests on the advection scheme are necessary and will be the subject of a following study.

3.2. Multigrid method

The flow solver (conservation of mass and momentum) is decoupled from the treatment of the energy equation: the velocity field computed at time-step (n) is used for the advection of heat in the computation of temperature at time ($n + 1$). The pressure and velocity fields are then updated simultaneously using the new temperature field to compute buoyancy and viscosity. The coupling of velocity and pressure fields is inspired by the PISO algorithm (pressure implicit with splitting operators [14]).

3.2.1. Multigrid algorithm

Discrete elliptic equations (11), (12), (16), (19) are solved using a multigrid algorithm. The principle of these methods first introduced by Brandt [7] is to reduce the longer wavelengths of the error of the solution, converging very slowly on meshes with a large number of grid points on coarser grids where computation is cheaper. Convergence rates of multigrid schemes are shown to be independent of the problem size. A precise presentation of the various multigrid schemes can be found in [28]. We use a method initially designed for non-linear systems: the full approximation storage (FAS) algorithm [7]. This version increases the precision of coarse grid correction by solving for the relative truncation error of the fine grid operator.

3.2.2. Smoother

Among simple iterative methods, a basic Gauss–Seidel smoother is proposed, providing good results. The convergence speed of several classical multigrid algorithm have been tested (V cycles, W cycles and full-multi grid algorithm) indicating that V cycles are noticeably cheaper, though more complex multigrid cycles appear more stable at high viscosity contrasts (reflecting earlier results in a 3D Cartesian geometry [1]).

3.2.3. Transfer operators

Simple transfer operators (restriction and prolongation) are also adopted. Concerning the restriction from a given grid to a coarser grid, an arithmetic average involving four discrete neighboring values for velocities (eight for pressure) is used. The prolongation is a (tri)-linear interpolation (from eight neighboring values on the coarser grid for pressure, four for velocities). In order to keep integer weights in the averaging process, curvature distortions are neglected, assuming that the grid mesh is regular in each direction.

3.2.4. Coarse grid operators

Finally, the operators used for coarse grid approximation are simply derived from the fine grid discretization so that the linear system is basically identical to (11), (12), (16), and (19). This approach has been preferred for its simplicity to more complex algebraic operators such as the Galerkin coarse grid approximation where the system solved on coarser grids depends on the transfer operators. Thus, viscosity is also computed on coarser grid assuming linear variations of temperature between grid points (i.e. a geometric average of finer grid values of viscosity is used).

3.2.5. Performance

In summary, simple multigrid tools (Gauss–Seidel smoother, V cycles, linear transfer operators, discretization coarse grid approximation) have been selected for this problem. More sophisticated tools might

improve the performance as found in the Cartesian case [3,26]. The simplicity (and relatively low CPU cost) of the selected features turn out to be a good approach when both efficiency and stability criterions are considered. Fig. 3 demonstrates in the isoviscous context that the present implementation provides results close to the theoretical characteristic of multigrid performance: the number of V-cycles needed to achieve a given convergence criterion is almost independent of the grid size so that the relationship between CPU time and mesh size is close to linear.

The optimum number of coarse grid corrections (i.e. the number of coarse grids used in addition to the finest grid) has a value of about 4, relatively independent of the viscosity gradients (cf. Table 1). However, when the viscosity contrast is increased, the number of smoothing steps N_y on each grid needs to be increased for a better performance (for the largest viscosity contrasts investigated, too small values of N_y do not allow the convergence of the multgrid algorithm...). Note that data presented in Table 1 is only an indication of the behavior of the program when viscosity becomes more variable. The algorithm is sensitive to (local) viscosity gradients so that the global contrast has no quantitative signification. Fortunately, in thermal convection problems, diffusion of heat smoothes the temperature distribution: the maximum viscosity jump between two adjacent cells of the 64^3 grid mesh in the $a_{\mathrm{vis}} = 12$ case in Table 1 is about 60. In the context of planetary interiors, sharper viscosity jumps associated to a compositional boundary or to the localization of deformation associated to plate tectonics, might cause more trouble to the present algorithm. Due to the absence of an initial guess for the velocity and pressure fields in the cases presented in Table 1, it must be emphasized that a more realistic computational procedure (e.g. increasing the viscosity parameter a_{vis} from one calculation to the other and using the previous result as a start) allows to reach global viscosity contrasts of 10^6 ($a_{\mathrm{vis}} = 14$) at a reasonable computation cost.

3.3. Parallel implementation and boundary conditions

The main interest of the cubed sphere gridding technique is that all six regions composing the sphere have an identical geometric structure and thus, the same metric. Again, I focus here on the parallel method

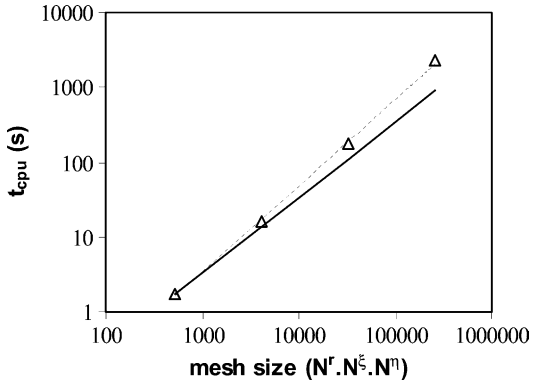

Fig. 3. Influence of the grid size ($N^r \cdot N^\xi \cdot N^\eta$) on the convergence rate of the flow solver measured by the CPU time (t_{cpu}, in s) elapsed to achieve a given convergence criterion (relative pressure and velocity residuals smaller than 10^{-5}). The straight line indicates a theoretical linear increase (slope 1). The dashed line is a power-law fit of the data (slope 1.15). A single time-step is performed from a temperature field corresponding to a conductive solution perturbed with a random distribution of amplitude 10^{-3} ($Ra_T = 10^6$, $\tilde{H} = 0$, $\rho = 0.5$). Initial velocity and pressure fields are set to zero. Optimum multigrid parameters have been selected. These tests have been performed on a single CPU (Pentium IV 2.4 GHz).

Table 1
Influence of the viscosity contrast on the solver's performance on a 64^3 grid mesh ($Ra_T = 10^6$, $\rho = 0.5$)

$\Delta\mu$	N_y	m	N_{cy}	t_{cpu} (s)
1.63×10^5	20	4	12	130
2.20×10^4	13	4	10	71.0
2.98×10^3	11	4	8	50.3
4.03×10^2	4	4	11	28.2
5.46×10^1	4	4	8	20.9
10^0	4	5	5	14.9

$\Delta\mu$ is the global viscosity contrast (values obtained from the following values of a_{vis}: 12, 10, 8, 6, 4, 0). N_y is the number of smoothing steps on each grid. m is the number of coarser grids used in the multigrid V-cycles. Optimum values for (N_y,m) have been selected (the criterion is the minimum number of equivalent fine grid iterations). N_{cy} is the number of V-cycles needed to obtain relative residuals of velocity and pressure that are smaller than 10^{-3} from an arbitrary temperature field (snapshot of a time-dependent steady-state obtained for $a_{vis} = 8$ and no internal heat sources) and arbitrary initial velocity and pressure solutions (V and p are set to 0 initially). t_{cpu} is the CPU time on a 8 processes PC cluster (Pentium IV 2.4 GHz).

used for one sixth of the shell. The future coupling to the five other blocks and its parallel implementation are well described by Ronchi et al. [18], proving the efficiency of their method.

3.3.1. *Process' grid*

The method is similar to what could be used for a rectangular grid: the global mesh is decomposed in a 'process' grid with $M^r \cdot M^\xi \cdot M^\eta$ local ('process') meshes. For simplicity, the program is designed to handle a decomposition with a number of processes in each direction that is a power of 2; in order to allow a maximum number of coarse grid operations, the size of the global mesh used in the calculations also treats number of cells in the three directions that are powers of 2 (though a direction with a number of cells such as $p \cdot 2^q$ with p an odd number, allowing for q coarse grid corrections, at least in this direction, could also be used). Buffer planes are added to this local mesh in each direction that allow the storage of data needed for the computation of the discrete schemes presented in paragraph 3.1: either the boundary is a 'virtual' boundary induced by the spatial decomposition of the problem into several distinct processes, either it is a physical boundary of the problem.

3.3.2. *Parallel communication*

In the case of a virtual boundary, the MPI library is used to fill in the buffers. Buffers for a given variable (temperature, pressure or velocity component) are updated on all local meshes once a new value has been computed e.g. at the end of the diffusion-advection step for temperature, once θ^{n+1} is available on all local meshes, or after one smoothing step for one of the projections of the momentum equation corresponding to updating a single velocity component among the three. Note that the effective smoothing performed during the calculation thus differs slightly from the Gauss–Seidel method since values of the previous relaxation step are used to compute the discrete stencil on points neighboring virtual boundaries. One 2D plane is exchanged among adjacent processes (unless one side of the local 'process' domain is included in one boundary of the global domain).

3.3.3. *Performance*

Fig. 4 indicates the efficiency of the parallel implementation. Up to eight processes, the gain is close to perfect: the product of CPU time by the number of processes does not vary with the process grid size. This

feature deteriorates for larger process grids (reflecting a similar behavior of Cartesian programs): this is due to a combination of the machine's architecture and the fact that for a given mesh size (64^3 in the case presented in Fig. 4), too large process grids induce a less interesting theoretical ratio for communication time between processes over computation time. Tests further indicate that no absolute gain is provided by the use of a larger number of process if the number of cells of a local 'process' mesh in one direction is smaller than 16. Larger process grids should thus be associated to larger meshes.

3.3.4. Boundary conditions

Physical boundaries are also treated with the 'buffer planes' technique. A Dirichlet boundary condition for temperature or velocity is set by prescribing a linear variation of the variable between the discrete points closest to the boundary (equidistant to it) that coincides with the boundary value on the boundary plane: for example, assuming T^* is prescribed on plane $\eta = -\pi/4$, the boundary condition is written $T^0 = 2T^*(\Delta V^*/\Delta V^0) - T^1(\Delta V^1/\Delta V^0)$ with ΔV^*, ΔV^0, ΔV^1, control volume values associated to discrete values T^*, T^0, T^1 (the same is valid for velocity components tangent to the plane). Note that the volume ratios are reasonably small for adjacent cells in a fine enough grid mesh. In the case of normal velocity V^η, the Dirichlet boundary condition is a mass flux prescription that is handled directly in the flow solver: velocity values V^η are not modified on this plane... For a Neumann boundary condition, a prescribed dimensionless heat flux f^* (which may be an adiabatic condition) is written $T^0 = f^*\Delta l^{\eta *} + T^1$, where $\Delta l^{\eta *} = (\Delta l^\eta_{i,j,0} + \Delta l^\eta_{i,j,1})/2$ is the distance between the two discrete points (the same is valid for velocity components tangent to the plane). Finally, periodic boundary conditions can be imposed (especially in the ξ and η directions for thermal convection) using the communication between processes: 'torus' exchange is prescribed corresponding to an extended definition of the 'down' and 'up' neighbors. Since one of the coordinates does not coincide on adjacent blocks, a subsequent 1D interpolation is needed (see Fig. 5). In the case of vector variables (here, velocities), appropriate recomputations of the components are performed. Consider block ($x > 0$) in Fig. 1 for example: periodicity at the (ξ = constant) boundaries implies that the flow out of plane ($\xi = \pi/4$, right), enters through plane ($\xi = -\pi/4$, left) with a coordinate system associated to the adjacent block ($y < 0$) (Fig. 1). In this example, the link between velocity components on the boundary is

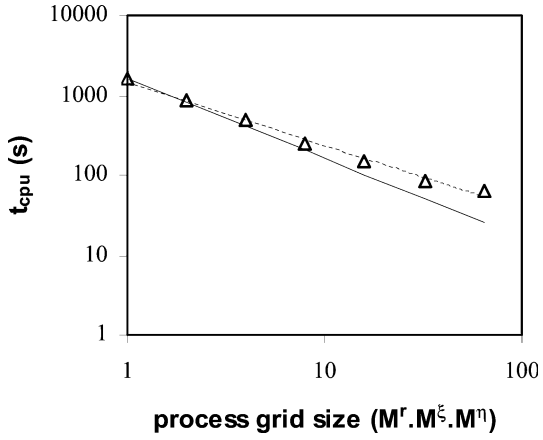

Fig. 4. Efficiency of the parallel implementation indicated by the CPU time (t_{cpu}, in s) as a function of the size of the process grid ($M^r \cdot M^\xi \cdot M^\eta$). Same case than in Fig. 5 for a 64^3 mesh. The straight line indicates an inversely proportional decrease (slope-1). The dashed line is a power law fit of the data (slope -0.8). These tests have been performed on a SGI O3800 machine (768 R14000/500 MHz processors).

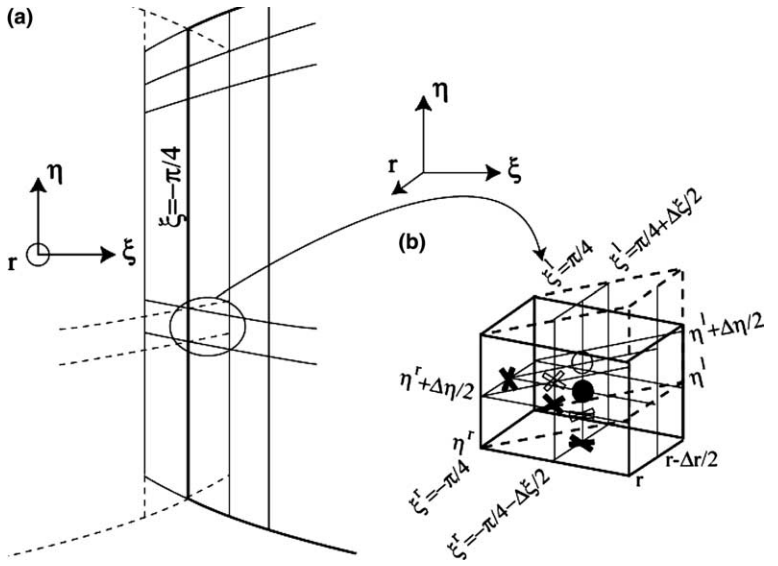

Fig. 5. Interpolation between adjacent blocks. (a) Global configuration of coordinate lines: consider the spherical surface corresponding to one of the six blocks (bold lines, *right block r*). The adjacent block at boundary $\xi = -\pi/4$ (dashed lines, *left block l*) shares two of the cubed sphere coordinates (r and ξ); however, the remaining coordinate (η) does not coincide on both blocks. (b) Discrete positioning of the staggered grid at the boundary: a 1D interpolation is needed to pass velocities and temperature values from one block to the other. Again the cell belonging to the right block is delimited with bold lines, the left block cell, with dashed lines. Velocity positions are indicated with crosses (filled for the right block, empty for the left block), and the temperature positions with spheres. A third coordinate system (e.g. Cartesian coordinates) can be used to compare the locations associated to $(\eta^l,\eta^l + \Delta\eta/2)$ and $(\eta^r,\eta^r + \Delta\eta/2)$ at angle $\xi^r = -\pi/4 - \Delta\xi/2$ (or $\pi/4 + \Delta\xi/2$ for ξ^l) and radii r and $r + \Delta r/2$.

$$V'^{\xi} = \frac{\sqrt{1+\frac{Y^2}{X^2}}}{D} V^{\xi},$$
$$V'^{\eta} = V^{\eta} - \frac{CY}{DX} V^{\xi}, \tag{23}$$

where primes denote values on the right plane. Obviously, periodic boundaries in the ξ and η directions mimic the interpolation procedures that should be used in the context of the whole spherical shell to exchange boundary values between adjacent blocks among the six composing the sphere. These procedures shall be exposed in more details in a later study dealing with the whole shell.

4. Results

Due to the absence of relevant benchmark cases for 3D convection in a spherical shell with strongly variable viscosity, I propose two kinds of tests suitable for my program: first, simple 'shear' cases for the flow solver. Then, for the global convection problem, mean scalar values are reported on some cases that can be compared to existing data in the case of an isoviscous fluid.

4.1. Flow solver

For an isoviscous fluid, the flow resulting from the rotation of the two spheres bounding the surface ($r = \rho$ and $r = 1$) is [16]

$$\bar{V} = \frac{\rho^3}{1-\rho^3}\left\{\left(\frac{1}{r^3}-1\right)\bar{\Omega}_1 \otimes \bar{r} + \left(\frac{1}{\rho^3}-\frac{1}{r^3}\right)\bar{\Omega}_2 \otimes \bar{r}\right\} \tag{24}$$

where $\bar{\Omega}_1$(resp. $\bar{\Omega}_2$) is the rotation vector associated to the internal (respectively external) spherical boundary. For unit rotation vectors aligned with Cartesian axis y and z: $\bar{\Omega}_1 = (0,1,0)_{xyz}$ and $\bar{\Omega}_2 = (0,0,1)_{xyz}$, the solution velocity field is thus in the cubed sphere coordinate system:

$$\begin{aligned}
\tilde{V}^r &= 0,\\
\tilde{V}^\xi &= \frac{\rho^3}{r^2\delta(1-\rho^3)}\left[XYD\left(r^3-1\right) + C^2D\left(\frac{r^3}{\rho^3}-1\right)\right],\\
\tilde{V}^\eta &= \frac{\rho^3}{r^2\delta(1-\rho^3)}\left[D^2C\left(r^3-1\right) + XYC\left(\frac{r^3}{\rho^3}-1\right)\right].
\end{aligned} \tag{25}$$

A similar shear solution can also be obtained in the case of a viscosity that is only radius-dependent: for simplicity, it can be considered that in the classical spherical coordinate system (r,ϕ,θ), the flow resulting from the rotation of the outer sphere $\bar{\Omega}_2 = (0,0,1)_{xyz}$ (the lower limit remaining fixed, $\bar{\Omega}_1 = \bar{0}$) results in a single non-zero component along the ϕ-coordinate direction (in the example of an isoviscous fluid, $\tilde{V}^\phi = (r/(1-\rho^3) - \rho^3/r^2(1-\rho^3))\sin\theta$). Similarly, if viscosity is a function $\mu(r)$ of radius r only, there is a flow solution with a single non-zero component in the spherical coordinate system; such as the stress quantity $\mu(r)r^4(\tilde{V}^\phi/r)_{,r}$ is only a function of colatitudes θ. In the case of a parabolic increase of viscosity from the inner sphere towards the outer sphere, $\mu(\mathrm{r})=(\mathrm{r}/\rho)^2$, the velocity solution is, in the cubed sphere coordinate system,

$$\begin{aligned}
\tilde{V}^r &= 0,\\
\tilde{V}^\xi &= \left(\frac{r}{1-\rho^5} - \frac{\rho^5}{r^4(1-\rho^5)}\right)C^2D/\delta,\\
\tilde{V}^\eta &= \left(\frac{r}{1-\rho^5} - \frac{\rho^5}{r^4(1-\rho^5)}\right)CXY/\delta.
\end{aligned} \tag{26}$$

Fig. 6 displays the two cases corresponding to Eqs. (25) and (26). In both cases, the flow solver returns results as close as required to the theoretical solution (the obtained velocity fields differ both from the exact solutions by less than 1% for a 32^3 mesh). In order to further test our implementation by introducing a coupling with a non-zero velocity component in the r-direction, an arbitrary velocity field satisfying the problem such as $\tilde{V}^r = r^{-2}$ can be added to the above cases (thus imposing a mass flux through the spherical boundaries). Again, the flow solver provides an exact answer.

4.2. Thermal convection

Two test cases are proposed:

1. Approximation of the critical Rayleigh number for a spherical shell from a linear stability analysis [9] with $\rho = 0.5$ and free-slip boundaries provides the value 1102.5 (for Ra_T defined with the thickness of the shell) for a spherical harmonics disturbance of order 2, no internal heat sources and a constant gravity. Calculations on one sixth of the sphere with periodic lateral boundaries and a similar perturbation provides a value of 1095 for a mesh containing 32^3 grid cells, very close to the prediction (i.e. an error of about 0.7%).

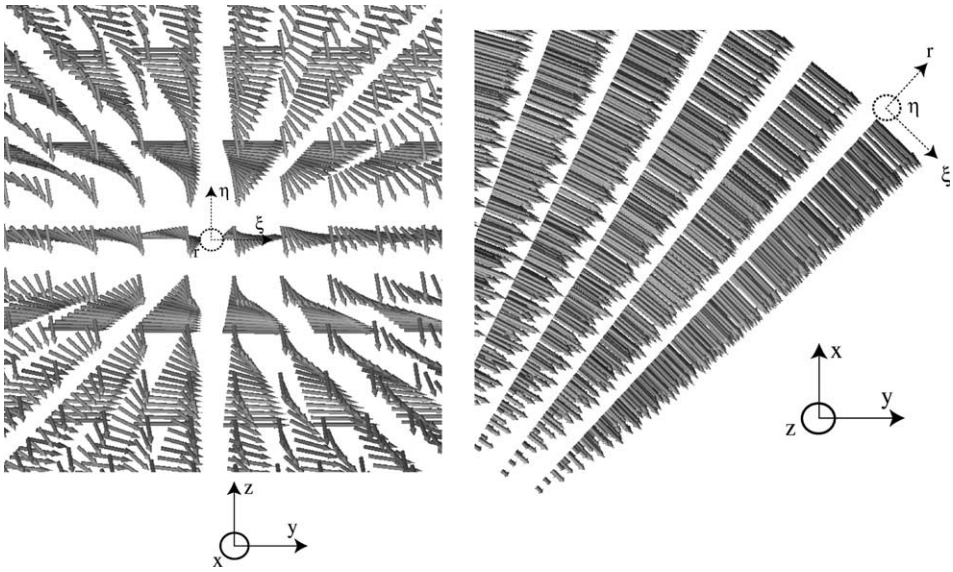

Fig. 6. Test cases for the flow solver (details of the flow). Arrows (length and direction) denote the velocity field computed from prescribed boundary velocities. The Cartesian coordinate system as well as the local directions of the cubed sphere coordinate system at a given location are presented. Left: prescribed unit rotation of the outer sphere along the z-axis and of the inner sphere along the y-axis; view from $(0,0,0)_{xyz}$. The fluid is isoviscous. Right: prescribed unit rotation of the outer sphere along the z-axis, inner sphere being fixed. Radius-dependent viscosity ($\mu(r) = (r/\rho)^2$); view from $(0,0,z_0 > 0)_{xyz}$.

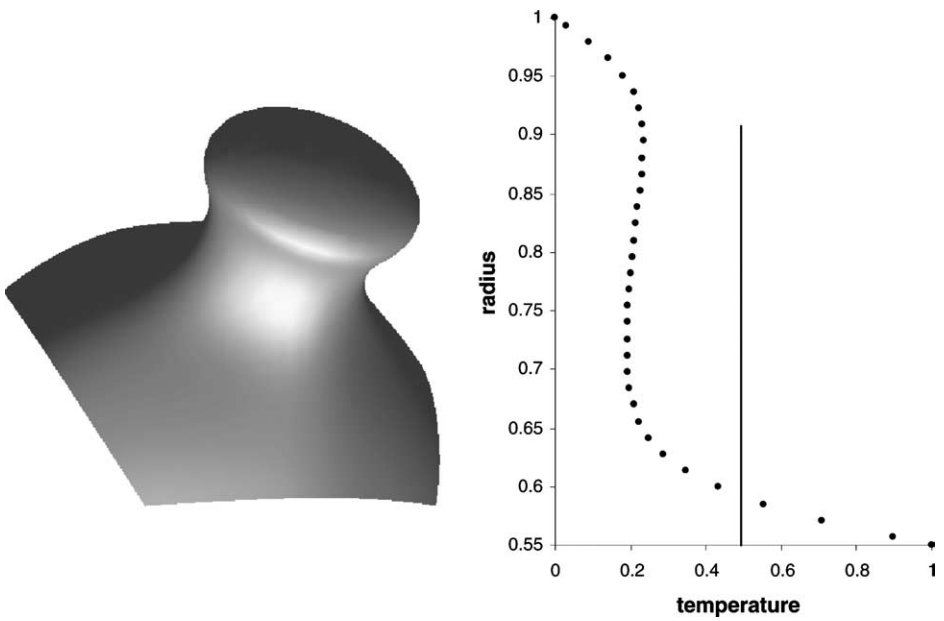

Fig. 7. Steady convection ($Ra_T = 1.4 \times 10^3$, $a_{vis} = 0$), 32^3 grid cells, free slip spherical boundaries, periodic azimuthal boundaries. Left: isosurface corresponding to the 0.5 value (hot boundary layer). Right: radial profile of the temperature. The vertical line indicates the isosurface value.

2. A result for fully developed steady isoviscous thermal convection ($Ra_T = 1.4\ 10^3$, $a_{vis} = 0$) is presented in Fig. 7. Temperatures are prescribed on the two spherical boundaries with no internal heat sources ($\tilde{H} = 0$). Periodic conditions are associated to the four planar boundaries ($\xi = \pm\pi/4$) and ($\eta = \pm\pi/4$) and free-slip is prescribed on the spherical surfaces. This result corresponds to one sixth of the cubic solution described earlier by Bercovici et al. [6] or Ratcliff et al. [17]. The Nusselt numbers associated to this calculation are 4.40 at the surface and 4.45 at the bottom, compared to a surface value of 4.4449 obtained by Ratcliff et al. [17].

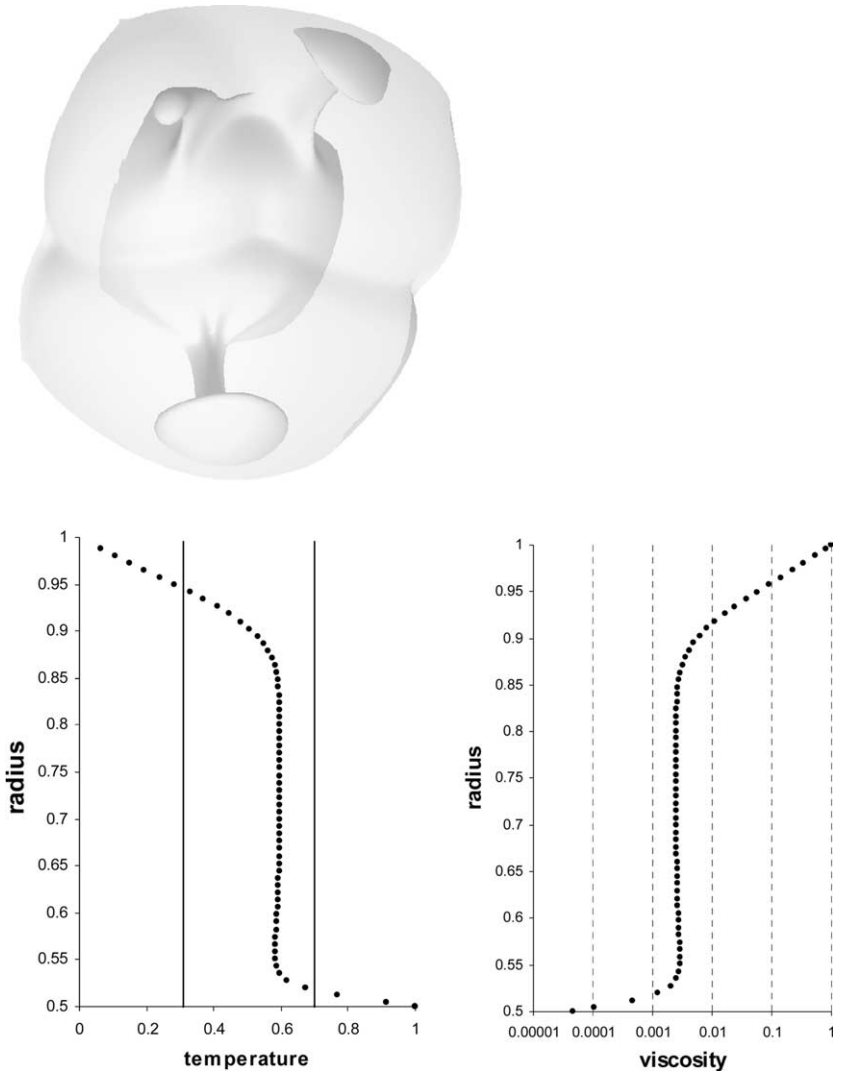

Fig. 8. Time-dependent stagnant lid convection ($Ra_T = 10^3$, $a_{vis} = 10$), 64^3 grid cells, free slip spherical boundaries, periodic azimuthal boundaries. Left: isosurfaces corresponding to $\theta = 0.3$ (transparent, bottom of the lid) and $\theta = 0.7$ (hot boundary layer). Center: radial profile of the temperature. The vertical lines indicate the isosurface values. Right: radial profile for the viscosity.

Finally, Fig. 8 displays a snapshot of a time-dependent calculation in the stagnant lid regime ($Ra_T = 10^3$, $a_{vis} = 10$). Note that, unlike the Cartesian case (e.g. [20]), the viscosity variations in a spherical layer are not confined to the cold stagnant lid: since the hot boundary layer still has a significant amplitude, it is associated to viscosity variations of almost two orders of magnitude. This large temperature difference controlling the birth of hot instabilities, characteristic of the spherical shell should be one of the main themes for thermal convection studies in this geometry.

5. Conclusions

1. The numerical procedure presented here is based on numerical schemes providing the most efficient treatment of thermal convection with strongly variable viscosity in a 3D Cartesian geometry (e.g. [1]). The choice of the 'cubed sphere' gridding technique ensures minimal modifications when transferring these finite volume methods to the case of a spherical geometry since it provides a mesh reasonably close to uniform. The present study only deals with a single block corresponding to one sixth of the spherical shell. However, the numerical treatment of the same equations on the full shell is straightforward and has already been proven to be very efficient in the isoviscous case [12].
2. The equations are written directly in the 'cubed sphere' coordinate system. A staggered grid mesh is used with contravariant components of velocities and stress. Since coordinates are not orthogonal, the convection equations and the associated discrete formulation exhibit a slightly higher complexity inducing an increase of CPU cost (and, to a lesser extent, of memory) in comparison to the Cartesian context.
3. Furthermore, simplifications inherent to the multigrid algorithm in the flow solver (mainly because spherical distortions are neglected in the restriction and prolongation operators for simplicity) make it slightly less efficient than in the Cartesian case. However, even in the Cartesian case, the poor representation of large viscosity gradients on too coarse grids limits the efficiency of the multigrid algorithm when the fine grid discretization is used as a coarse grid operator (more sophisticated methods might improve this aspect). Thus, the number of coarse grid corrections should be reduced in that case. However, these simple features (Gauss–Seidel smoother, V cycles, linear prolongation and restriction) are proven here to be efficient and robust for a global viscosity contrasts up to 10^6, at a reasonable cost.
4. The parallel implementation is simple (though an additional specific treatment should be implemented when dealing with the six blocks constituting the whole sphere, as proposed by Ronchi et al. [18]). If local 'process' meshes are large enough, it is very efficient. Boundary conditions are formulated in a simple way, using the same buffer planes than those used for communications between processes. The case of periodic boundary conditions in the ξ and η directions is more sophisticated than Dirichlet or Neumann conditions: appropriate interpolations and re-computation of the vector components are performed in this case.
5. Further developments should be proposed concerning the numerical treatment of the advection-diffusion equation for the energy conservation. Advection schemes with large numerical diffusion induce anisotropic distortions. The benchmarking of advection schemes is the subject of a second paper.
6. In conclusion, the 'cubed sphere' provides a good mesh to implement the numerical resolution of thermal convection with variable viscosity fluids in a spherical geometry. The two major paths for future studies in the dynamics of planetary interiors concern rheology (the nature of plate tectonics and many related topics in geodynamics, the role of partial melting) and composition (its influence on dynamical regimes): the present numerical method is designed to handle large viscosity contrasts so that more complex rheologies may be implemented from this version proposed for temperature-dependent viscosity; in addition, classical techniques allowing the description of the convective dynamics of two immiscible fluids

of different density and viscosity (e.g. the use of particle tracers) can be implemented in the same way they are treated in a 3D Cartesian geometry. Thus, studies of the internal dynamics of planets should benefit from the present numerical model.

Acknowledgments

I thank Stéphane Labrosse for giving the idea of the cubed sphere and P. Tackley and P. Wesseling for useful comments on an earlier version of the manuscript.

Appendix A. Deriving convective equations in the 'cubed' sphere coordinate system

The natural basis $(\bar{e}_r, \bar{e}_\xi, \bar{e}_\eta)$ associated to the cubed sphere coordinate system (r,η,ξ) at point M is, by definition: $\bar{e}_r = \frac{\partial \overline{OM}}{\partial r}$, $\bar{e}_\xi = \frac{\partial \overline{OM}}{\partial \xi}$, $\bar{e}_\eta = \frac{\partial \overline{OM}}{\partial \eta}$. Note that the matrix passing from the Cartesian coordinates basis $(\bar{e}_x, \bar{e}_y, \bar{e}_z)$ to this natural basis is (Fig. 1),

$$\begin{bmatrix} \frac{1}{\sqrt{\delta}} & \frac{X}{\sqrt{\delta}} & \frac{Y}{\sqrt{\delta}} \\ \frac{-rXC^2}{\delta^{3/2}} & \frac{rC^2D^2}{\delta^{3/2}} & \frac{-rXYC^2}{\delta^{3/2}} \\ \frac{-rYD^2}{\delta^{3/2}} & \frac{-rXYD^2}{\delta^{3/2}} & \frac{rC^2D^2}{\delta^{3/2}} \end{bmatrix} \tag{A.1}$$

The Cristoffel coefficients Γ^k_{ij} are introduced to describe the variations of the natural basis with location M: $\frac{\partial \bar{e}_i}{\partial x^j} = \Gamma^k_{ij}\bar{e}_k$. The following expressions are obtained:

$$\left\{ \begin{array}{ccc} \Gamma^r_{rr} = 0, \Gamma^\xi_{rr} = 0, \Gamma^\eta_{rr} = 0 & \Gamma^r_{r\xi} = 0, \Gamma^\xi_{r\xi} = \frac{1}{r}, \Gamma^\eta_{r\xi} = 0 & \Gamma^r_{r\eta} = 0, \Gamma^\xi_{r\eta} = 0, \Gamma^\eta_{r\eta} = \frac{1}{r} \\ \dots & \Gamma^r_{\xi\xi} = \frac{-rC^4D^2}{\delta^2}, \Gamma^\xi_{\xi\xi} = \frac{2XY^2}{\delta}, \Gamma^\eta_{\xi\xi} = 0 & \Gamma^r_{\xi\eta} = \frac{rC^2D^2XY}{\delta^2}, \Gamma^\xi_{\xi\eta} = \frac{-D^2Y}{\delta}, \Gamma^\eta_{\xi\eta} = \frac{-C^2X}{\delta} \\ \dots & \dots & \Gamma^r_{\eta\eta} = \frac{-rC^2D^4}{\delta^2}, \Gamma^\xi_{\eta\eta} = 0, \Gamma^\eta_{\eta\eta} = \frac{2X^2Y}{\delta} \end{array} \right\}. \tag{A.2}$$

The nine remaining coefficients are obtained from symmetry, since $\Gamma^k_{ij} = \Gamma^k_{ji}$ due to the continuity of $\overline{OM}$ and its derivatives. The divergence of a vector $\bar{V}$ is therefore

$$\overline{\nabla} \cdot \bar{V} = V^i_{,i} + V^k\Gamma^i_{ki} = \frac{1}{r^2}(r^2V^r)_{,r} + V^\xi_{,\xi} + \frac{X(2Y^2 - C^2)V^\xi}{\delta} + V^\eta_{,\eta} + \frac{Y(2X^2 - D^2)V^\eta}{\delta}. \tag{A.3}$$

(Note the use of contravariant components for the velocity vector in this problem.)

In order to compute the stress tensor, the expression of the gradient of a vector field is needed: the 1-contravariant, 2-covariant components of this second order tensor are $(\overline{\nabla V})^j_i = V^j_{,i} + V^k\Gamma^j_{ik}$ so that

$$\left[(\overline{\nabla V})^\bullet_\bullet\right] = \begin{bmatrix} V^r_{,r} & V^r_{,\xi} + V^\xi\frac{-rC^4D^2}{\delta^2} + V^\eta\frac{rC^2D^2XY}{\delta^2} & V^r_{,\eta} + V^\eta\frac{-rC^2D^4}{\delta^2} + V^\xi\frac{rC^2D^2XY}{\delta^2} \\ \frac{1}{r}(rV^\xi)_{,r} & V^\xi_{,\xi} + V^r\frac{1}{r} + V^\xi\frac{2XY^2}{\delta} + V^\eta\frac{-D^2Y}{\delta} & \sqrt{\delta}\left(\frac{V^\xi}{\sqrt{\delta}}\right)_{,\eta} \\ \frac{1}{r}(rV^\eta)_{,r} & \sqrt{\delta}\left(\frac{V^\eta}{\sqrt{\delta}}\right)_{,\xi} & V^\eta_{,\eta} + V^r\frac{1}{r} + V^\xi\frac{-C^2X}{\delta} + V^\eta\frac{2X^2Y}{\delta} \end{bmatrix}. \tag{A.4}$$

Given the contravariant components of the metric tensor,

$$[g^{\bullet\bullet}] = \begin{bmatrix} 1 & 0 & 0 \\ 0 & \frac{\delta}{r^2C^2} & \frac{\delta XY}{r^2C^2D^2} \\ 0 & \frac{\delta XY}{r^2C^2D^2} & \frac{\delta}{r^2D^2} \end{bmatrix} \tag{A.5}$$

the contravariant components of the stress tensor $\bar{\bar{\tau}} = \mu[(\overline{\nabla V}) + (\overline{\nabla V})^t]$ are thus,

$$\begin{aligned}
\tau^{rr} &= 2\mu V^r{}_{,r}, \\
\tau^{r\xi} &= \mu\left(V^\xi{}_{,r} + \frac{\delta}{r^2C^2}V^r{}_{,\xi} + \frac{\delta XY}{r^2C^2D^2}V^r{}_{,\eta}\right), \\
\tau^{r\eta} &= \mu\left(V^\eta{}_{,r} + \frac{\delta}{r^2D^2}V^r{}_{,\eta} + \frac{\delta XY}{r^2C^2D^2}V^r{}_{,\xi}\right), \\
\tau^{\xi\xi} &= 2\mu\left(\frac{\delta XY}{r^2C^2D^2}V^\xi{}_{,\eta} + \frac{\delta}{r^2C^2}V^\xi{}_{,\xi} + \frac{\delta}{r^3C^2}V^r + \frac{-D^2Y}{r^2C^2}V^\eta + \frac{XY^2}{r^2C^2}V^\xi\right), \\
\tau^{\eta\eta} &= 2\mu\left(\frac{\delta XY}{r^2C^2D^2}V^\eta{}_{,\xi} + \frac{\delta}{r^2D^2}V^\eta{}_{,\eta} + \frac{\delta}{r^3D^2}V^r + \frac{-C^2X}{r^2D^2}V^\xi + \frac{X^2Y}{r^2D^2}V^\eta\right), \\
\tau^{\xi\eta} &= \mu\left(\frac{\delta^{3/2}}{r^2C^2}\left(\frac{V^\eta}{\sqrt{\delta}}\right)_{,\xi} + \frac{-\delta XY}{r^2C^2D^2}V^r{}_{,r} + \frac{\delta^{3/2}}{r^2D^2}\left(\frac{V^\xi}{\sqrt{\delta}}\right)_{,\eta}\right).
\end{aligned} \tag{A.6}$$

Finally, in order to write the conservation of momentum, the expression of the divergence of the second order tensor $\bar{\bar{\tau}}$ is needed. Its contravariant components in the natural basis are $(\overline{\nabla} \bullet \bar{\bar{\tau}})^i = \tau^{ik}_{,k} + \tau^{mk}\Gamma^i_{mk} + \tau^{im}\Gamma^k_{mk}$, so that

$$\left(\overline{\nabla} \bullet \bar{\bar{\tau}}\right)^r = \frac{1}{r^3}\left(r^3\tau^{rr}\right)_{,r} + \frac{\delta^{3/2}}{D^2}\left(\frac{D^2\tau^{r\eta}}{\delta^{3/2}}\right)_{,\eta} + \frac{\delta^{3/2}}{C^2}\left(\frac{C^2\tau^{r\xi}}{\delta^{3/2}}\right)_{,\xi}, \tag{A.7}$$

$$\left(\overline{\nabla} \bullet \bar{\bar{\tau}}\right)^\xi = \frac{1}{r^4}\left(r^4\tau^{\xi r}\right)_{,r} + \frac{\delta^{5/2}}{C^4}\left(\frac{C^4\tau^{\xi\xi}}{\delta^{5/2}}\right)_{,\xi} + \frac{\delta^{5/2}}{D^2}\left(\frac{D^2\tau^{\xi\eta}}{\delta^{5/2}}\right)_{,\eta}, \tag{A.8}$$

$$\left(\overline{\nabla} \bullet \bar{\bar{\tau}}\right)^\eta = \frac{1}{r^4}\left(r^4\tau^{\eta r}\right)_{,r} + \frac{\delta^{5/2}}{D^4}\left(\frac{D^4\tau^{\eta\eta}}{\delta^{5/2}}\right)_{,\eta} + \frac{\delta^{5/2}}{C^2}\left(\frac{C^2\tau^{\xi\eta}}{\delta^{5/2}}\right)_{,\xi}. \tag{A.9}$$

The main interest of the natural basis is to provide analysis formulae that do not depend on the coordinate system, however, $(\bar{e}_r, \bar{e}_\xi, \bar{e}_\eta)$ are not unit vectors so that, for example, 'velocities' V^η and V^ξ have the dimension of a frequency. In the following, we will present equations within the physical basis (i.e. the normed basis issued from the natural basis): $(\tilde{\bar{e}}_r, \tilde{\bar{e}}_\xi, \tilde{\bar{e}}_\eta)$. The contravariant coordinates $(\tilde{V}^r, \tilde{V}^\xi, \tilde{V}^\eta)$ of a vector $\bar{V}$ (e.g. velocity field) in this physical basis are such that

$$\begin{aligned}
\tilde{V}^r &= V^r, \\
\tilde{V}^\xi &= \frac{rC^2D}{\delta}V^\xi, \\
\tilde{V}^\eta &= \frac{rCD^2}{\delta}V^\eta.
\end{aligned} \tag{A.10}$$

Similarly, the contravariant expression of the (second order) stress tensor is

$$
\begin{aligned}
\tilde{\tau}^{rr} &= 2\mu \tilde{V}^{r}_{,r},\\
\tilde{\tau}^{r\xi} &= \mu\left(r\left(\frac{\tilde{V}^{\xi}}{r}\right)_{,r} + \frac{D}{r}\tilde{V}^{r}_{,\xi} + \frac{XY}{rD}\tilde{V}^{r}_{,\eta}\right),\\
\tilde{\tau}^{r\eta} &= \mu\left(r\left(\frac{\tilde{V}^{\eta}}{r}\right)_{,r} + \frac{C}{r}\tilde{V}^{r}_{,\eta} + \frac{XY}{rC}\tilde{V}^{r}_{,\xi}\right),\\
\tilde{\tau}^{\xi\xi} &= 2\mu\left(\frac{XY}{r\delta^{1/2}}\left(\frac{\sqrt{\delta}\tilde{V}^{\xi}}{D}\right)_{,\eta} + \frac{D}{r}\tilde{V}^{\xi}_{,\xi} + \frac{C^2D^2}{r\delta}\tilde{V}^{r} + \frac{-CYD^2}{r\delta}\tilde{V}^{\eta}\right),\\
\tilde{\tau}^{\xi\eta} &= \mu\left(\frac{CD}{r\delta^{1/2}}\left(\frac{\sqrt{\delta}\tilde{V}^{\eta}}{C}\right)_{,\xi} + \frac{-XYCD}{\delta}\tilde{V}^{r}_{,r} + \frac{CD}{r\delta^{1/2}}\left(\frac{\sqrt{\delta}\tilde{V}^{\xi}}{D}\right)_{,\eta}\right),\\
\tilde{\tau}^{\eta\eta} &= 2\mu\left(\frac{XY}{r\delta^{1/2}}\left(\frac{\sqrt{\delta}\tilde{V}^{\eta}}{C}\right)_{,\xi} + \frac{C}{r}\tilde{V}^{\eta}_{,\eta} + \frac{C^2D^2}{r\delta}\tilde{V}^{r} - \frac{DXC^2}{r\delta}\tilde{V}^{\xi}\right).
\end{aligned}
\tag{A.11}
$$

The conservation of mass is then

$$
\frac{1}{r^2}\left(r^2\tilde{V}^{r}\right)_{,r} + \frac{\delta^{3/2}}{rDC^2}\left(\frac{\tilde{V}^{\xi}}{\delta^{1/2}}\right)_{,\xi} + \frac{\delta^{3/2}}{rCD^2}\left(\frac{\tilde{V}^{\eta}}{\delta^{1/2}}\right)_{,\eta} = 0. \tag{A.12}
$$

The three equations for the conservation of the momentum are

$$
-p_{,r} + \frac{1}{r^3}\left(r^3\tilde{\tau}^{rr}\right)_{,r} + \frac{\delta^{3/2}}{rCD^2}\left(\frac{\tilde{\tau}^{r\eta}}{\delta^{1/2}}\right)_{,\eta} + \frac{\delta^{3/2}}{rC^2D}\left(\frac{\tilde{\tau}^{r\xi}}{\delta^{1/2}}\right)_{,\xi} + f_r = 0, \tag{A.13}
$$

$$
\frac{-1}{r}\left(\frac{XY}{D}p_{,\eta} + Dp_{,\xi}\right) + \frac{1}{r^3}\left(r^3\tilde{\tau}^{\xi r}\right)_{,r} + \frac{\delta^{3/2}}{rC^2D}\left(\frac{\tilde{\tau}^{\xi\xi}}{\delta^{1/2}}\right)_{,\xi} + \frac{\delta^{3/2}}{rCD}\left(\frac{\tilde{\tau}^{\xi\eta}}{D\delta^{1/2}}\right)_{,\eta} = 0, \tag{A.14}
$$

$$
\frac{-1}{r}\left(\frac{XY}{C}p_{,\xi} + Cp_{,\eta}\right) + \frac{1}{r^3}\left(r^3\tilde{\tau}^{\eta r}\right)_{,r} + \frac{\delta^{3/2}}{rCD^2}\left(\frac{\tilde{\tau}^{\eta\eta}}{\delta^{1/2}}\right)_{,\eta} + \frac{\delta^{3/2}}{rCD}\left(\frac{\tilde{\tau}^{\eta\xi}}{C\delta^{1/2}}\right)_{,\xi} = 0. \tag{A.15}
$$

Concerning the conservation equation (3), the only differential expressions that are needed are the laplacian and gradient of scalar field T, and the scalar product. All these are provided by Ronchi et al. [18] for contravariant coordinates of the physical basis $(\tilde{\tilde{e}}_r, \tilde{\tilde{e}}_\xi, \tilde{\tilde{e}}_\eta)$:

$$
\nabla^2\theta = \frac{1}{r^2}\left(r^2\theta_{,r}\right)_{,r} + \frac{\delta}{r^2}\left[\frac{\theta_{,\xi\xi}}{C^2} + \frac{\theta_{,\eta\eta}}{D^2} + \frac{2XY}{C^2D^2}\theta_{,\xi\eta}\right], \tag{A.16}
$$

$$
\overline{\nabla}\theta = \theta_{,r}\tilde{\tilde{e}}_r + \frac{1}{r}\left(D\theta_{,\xi} + \frac{XY}{D}\theta_{,\eta}\right)\tilde{\tilde{e}}_\xi + \frac{1}{r}\left(\frac{XY}{C}\theta_{,\xi} + C\theta_{,\eta}\right)\tilde{\tilde{e}}_\xi. \tag{A.17}
$$

And since the covariant components of the metric tensor associated to $(\tilde{\tilde{e}}_r, \tilde{\tilde{e}}_\xi, \tilde{\tilde{e}}_\eta)$ are

$$
[\tilde{g}_{\bullet\bullet}] = \begin{bmatrix} 1 & 0 & 0 \\ 0 & 1 & \frac{-XY}{CD} \\ 0 & \frac{-XY}{CD} & 1 \end{bmatrix},
$$

$$\bar{V}\cdot\overline{\nabla}\theta=\theta_{,r}\tilde{V}^{r}+\frac{\delta}{rC^{2}D}\theta_{,\xi}\tilde{V}^{\xi}+\frac{\delta}{rCD^{2}}\theta_{,\eta}\tilde{V}^{\eta}. \tag{A.18}$$

A detailed introduction to tensor analysis can be found in [2].

Appendix B. Discrete formulation

Fig. 2 indicates the notations used for the formulation of the discrete stencil. Angles $\xi_j=-\pi/4+(j+1/2)\Delta\xi$ and $\eta_k=-\pi/4+(k+1/2)\Delta\eta$ denote the location of the center of the 'cubic' cell $C_{i,j,k}$ where discrete values of pressure, viscosity and temperature are positioned. Angle $\xi_j^-=\xi_j^-+\Delta\xi/2$ (respectively, angle $\eta_k^-=\eta_k^-+\Delta\eta/2$) refers to the location of the cell vertical (respectively, horizontal) wall where velocity component V^{ξ} (respectively, V^{η}) is positioned. Similarly, radius $r_i=-\pi/4+(j+1/2)\Delta\xi r_i$ denotes the location of the cell center and r_i^- the vertical wall where V^r is positioned.

Variable X_j (respectively X_j^-,Y_k,Y_k^-) refer to the tangent of ξ_j(resp.ξ_j^-,η_k,η_k^-). Similarly, variables C_j (respectively C_j^-,D_k,D_k^-) refer to angle ξ_j (respectively ξ_j^-,η_k,η_k^-). Several values for variable δ have been identified as indicated by the simple scheme on Fig. 2, in order to simplify the notations and computation:

$$\begin{aligned}
\delta^{\mathrm{I}}_{j,k}&=1+X_j^2+Y_k^2,\\
\delta^{\mathrm{II}}_{j,k}&=1+X_j^{-2}+Y_k^{-2},\\
\delta^{\mathrm{III}}_{j,k}&=1+X_j^{-2}+Y_k^2,\\
\delta^{\mathrm{IV}}_{j,k}&=1+X_j^2+Y_k^{-2}.
\end{aligned} \tag{B.1}$$

Note that all these angular values are invariant throughout the computation and through the r-direction: they should be tabulated in 1D-(ξ,η,X,Y,C,D) or 2D-(δ^{I},δ^{II}, δ^{III}, δ^{IV}) arrays with negligible memory cost, thus reducing the computation cost.

In order to simplify the notations, various values of viscosity are also indexed, corresponding to similar angular notations than δ (but viscosities are radius-dependent!): $\mu_{i,j,k}$ being located at the cell center, as the temperature is, we introduce the following averages,

$$\begin{aligned}
\mu^{\mathrm{II}}_{i,j,k}&=\left(\mu_{i,j,k}\cdot\mu_{i,j-1,k}\cdot\mu_{i,j,k-1}\cdot\mu_{i,j-1,k-1}\right)^{1/4},\\
\mu^{\mathrm{III}}_{i,j,k}&=\left(\mu_{i,j,k}\cdot\mu_{i,j-1,k}\cdot\mu_{i-1,j,k}\cdot\mu_{i-1,j-1,k}\right)^{1/4},\\
\mu^{\mathrm{IV}}_{i,j,k}&=\left(\mu_{i,j,k}\cdot\mu_{i,j,k-1}\cdot\mu_{i-1,j,k}\cdot\mu_{i-1,j,k-1}\right)^{1/4}.
\end{aligned} \tag{B.2}$$

Finally, infinitesimal lengths $\Delta l^{\bullet}$ in the three directions (r,ξ,η) are needed to compute the advection scheme for the conservation of energy:

$$\begin{aligned}
\Delta l^{r}_{i,j,k}&=\Delta r,\\
\Delta l^{\xi}_{i,j,k}&=\frac{r_i C_j^2 D_k\Delta\xi}{\delta_{j,k}},\\
\Delta l^{\eta}_{i,j,k}&=\frac{r_i D_k^2 C_j\Delta\eta}{\delta_{j,k}}.
\end{aligned} \tag{B.3}$$

The area and volume of discrete elements are needed, for example, to compute spatial averages (such as radial temperature profiles) or in the case of boundary conditions (see Section 3.3). By definition, the area of a surface element on the sphere is $\Delta S_{i,j,k}=\|\bar{e}_{\xi_{i,j,k}}\otimes\bar{e}_{\eta_{i,j,k}}\|\Delta\xi\Delta\eta$ so that

$$\Delta S_{i,j,k} = \frac{r_i^2 C_j^2 D_k^2}{\delta_{j,k}^{3/2}} \Delta\xi\Delta\eta. \tag{B.4}$$

The volume ΔV of parallelepipedic cell $C_{i,j,k}$ is linked to the Jacobian J: $\Delta V_{i,j,k} = J_{i,j,k}\Delta r\Delta\xi\Delta\eta$ with $J_{i,j,k} = \bar{e}_{r_{i,j,k}} \cdot (\bar{e}_{\xi_{i,j,k}} \otimes \bar{e}_{\eta_{i,j,k}})$, for example. Thus,

$$\Delta V_{i,j,k} = \frac{r_i^2 C_j^2 D_k^2}{\delta_{j,k}^{3/2}} \Delta r\Delta\xi\Delta\eta. \tag{B.5}$$

All the notations above have been introduced for a grid mesh with $N^\bullet$ cells in each direction ($N^r \cdot N^\xi \cdot N^\eta$ in total). Thus, $\Delta r = (1-\rho)/N^r$, $\Delta\xi = \pi/(2N^\xi)$, $\Delta\eta = \pi/(2N^\eta)$. In a more general way, one could refer to the size of the fine mesh (on which the temperature and flow fields solution are eventually computed) as being $N_0^\bullet$ cells in each direction. Then, coarser grids introduced in the multigrid algorithm used in the flow solver present $N_n^\bullet = N^\bullet/2^n$ ($n = 1,2,\ldots$) cells in each direction, and the related increments for the three coordinates: Δr_n, $\Delta\xi_n$, $\Delta\ \eta_n$. Discrete notations derived above are identical for all grids.

References

[1] M. Albers, A local mesh refinement multigrid method for 3D convection problems with strongly variable viscosity, J. Comput. Phys. 160 (2000) 126.
[2] R. Aris, Vectors, Tensors and the Basic Equations of Fluid Mechanics, Prentice-Hall, Englewood Cliffs, NJ, 1962.
[3] C. Auth, H. Harder, Multigrid solution of convection problems with strongly variable viscosity, Geophys. J. Int. 137 (1999) 793.
[4] J.R. Baumgardner, Three-dimensional treatment of convective flow in the Earth's mantle, J. Stat. Phys. 39 (1985) 501.
[5] D. Bercovici, The generation of plate tectonics from mantle convection, Earth Plan. Sci. Lett. 205 (2003) 107.
[6] D. Bercovici, G. Schubert, G.A. Glatzmaier, A. Zebib, Three dimensional convection in a spherical shell, J. Fluid Mech. 239 (1992) 683.
[7] A. Brandt, Multi-level adaptative solutions to boundary value problems, Math. Comp. 31 (1977) 333.
[8] E. Chaljub, Y. Capdeville, J.-P. Vilotte, Solving elastodynamics in a fluid–solid heterogeneous sphere: a parallel spectral element approximation on non-conforming grids, J. Comput. Phys. 187 (2003) 457.
[9] S. Chandrasekhar, Hydrodynamic and Hydromagnetic Stability, Oxford University Press, Oxford, 1961, p. 220.
[10] G. Choblet, Dynamique interne des planètes: apport de la modélisation 3D pour un fluide à rhéologie complexe, Thèse de doctorat, Université de Rennes, 1999.
[11] F.H. Harlow, J.E. Welch, Numerical calculation of time-dependent viscous incompressible flow of fluid with free surface, Phys. Fluid 8 (1965) 2182.
[12] J.W. Hernlund, P.J. Tackley, Three-dimensional spherical shell convection at infinite Prandtl number using the 'cubed sphere' method, in: K.J. Bathe (Ed.), Computational Fluid and Solid Mechanics 2003, Elsevier, Amsterdam, 2003, p. 931.
[13] A.T. Hsui, W.S. Yang, J.R. Baumgardner, A preliminary study of the effects of some flow parameters in the generation of poloidal and toroidal energies within a 3D spherical thermal convection system with variable viscosity, Pure Appl. Geophys. 145 (1995) 487.
[14] R.I. Issa, A.D. Gosman, A.P. Watkins, The computation of compressible and incompressible recirculating flow by a non-iterative implicit scheme, J. Comput. Phys. 62 (1986) 66.
[15] D. Komatitsch, J. Ritsema, J. Tromp, The spectral-element method, Beowulf computing, and three-dimensional seismology, Science 298 (2002) 1737.
[16] L.D. Landau, E.M. Lifshitz, Fluid Mechanics, Course of Theoretical Physics, vol. 6, Butterworth-Heinemann, Oxford, 1959, p. 65.
[17] J.T. Ratcliff, G. Schubert, A. Zebib, Steady tetrahedral and cubic patterns of spherical shell convection with temperature-dependent viscosity, J. Geophys. Res. 25 (1996) 25473.
[18] C. Ronchi, R. Iacono, P.S. Paolucci, The "cubed sphere": a new method for the solution of partial differential equations in spherical geometry, J. Comput. Phys. 124 (1996) 93.
[19] V.S. Solomatov, Scaling of temperature- and stress-dependent viscosity convection, Phys. Fluids 7 (1995) 266.
[20] V.S. Solomatov, L.-N. Moresi, Stagnant lid convection on Venus, J. Geophys. Res. 101 (1996) 4737.
[21] D.B. Spalding, A novel finite difference formulation for differential expressions involving both first and second order derivatives, Int. J. Numer. Meth. Eng. 4 (1972) 551.
[22] D.J. Stevenson, T. Spohn, G. Schubert, Magnetism and thermal evolution of the terrestrial planets, Icarus 54 (1983) 466.

[23] P.J. Tackley, Three-dimensional models of mantle convection: influence of phase transitions and temperature-dependent viscosity, Ph.D. Thesis, California Institute of Technology, Pasadena, 1994.
[24] P.J. Tackley, Self-consistent generation of tectonic plates in time-dependent, three-dimensional mantle convection simulations 1. pseudoplastic yielding, Geochem. Geophys. Geosyst. 1 (2000), 2000G000036.
[25] P.J. Tackley, Self-consistent generation of tectonic plates in time-dependent, three-dimensional mantle convection simulations 2. Strain weakening and asthenosphere, Geochem. Geophys. Geosyst. 1 (2000), 2000G000043.
[26] R.A. Trompert, U. Hansen, The application of a finite volume multigrid method to 3D flow problems in a highly viscous fluid with variable viscosity, Geophys. Astrophys. Fluid Dyn. 83 (1996) 261.
[27] P. Wesseling, Cell-centered multigrid for interface problems, J. Comput. Phys. 79 (1988) 85.
[28] P. Wesseling, An Introduction to Multigrid Methods, Wiley, New York, 1992.
[29] P. Wesseling, Principles of Computational Fluid Dynamics, Springer, Berlin, 2001.
[30] S. Zhong, M. Zuber, L. Moresi, M. Gurnis, Role of temperature-dependent viscosity and surface plates in spherical shell models of mantle convection, J. Geophys. Res. 105 (2000) 11063.